# Control of Spin-Wave Damping in YIG Using Spin Currents from Topological Insulators

Aryan Navabi,[1,*] Yuxiang Liu,[1] Pramey Upadhyaya,[2] Koichi Murata,[1] Farbod Ebrahimi,[3] Guoqiang Yu,[1] Bo Ma,[4] Yiheng Rao,[4] Mohsen Yazdani,[1] Mohammad Montazeri,[1] Lei Pan,[1] Ilya N. Krivorotov,[5] Igor Barsukov,[6] Qinghui Yang,[4] Pedram Khalili Amiri,[1] Yaroslav Tserkovnyak,[2] and Kang L. Wang[1]

[1]*Department of Electrical Engineering, University of California, Los Angeles, California 90095, USA*
[2]*Department of Physics and Astronomy, University of California, Los Angeles, California 90095, USA*
[3]*Inston Inc., Los Angeles, California 90095, USA*
[4]*State Key Laboratory of Electronic Thin Films and Integrated Devices, University of Electronic Science and Technology of China, Chengdu 610054, China*
[5]*School of Physics and Astronomy, University of California, Irvine, California 92697, USA*
[6]*Department of Physics and Astronomy, University of California, Riverside, California 92521, USA*

(Received 3 September 2018; revised manuscript received 3 February 2019; published 19 March 2019)

Spin waves in insulating materials such as Yttrium Iron Garnet (YIG) can be used for signal propagation and processing using the spin of the electrons rather than transport of their charge. Planar YIG films can be integrated with silicon technology to realize devices such as tunable filters, frequency selective limiters, and signal-to-noise enhancers. However, such films suffer from spin-wave damping, which limits their use in such applications. Here, we show that spin currents in topological insulators (TI) can be used to reduce spin-wave damping. TI supports surface spin currents, potentially making it an efficient source of antidamping torque. We show that in a YIG/$Bi_2Se_3$ bilayer, the spin-wave damping rate can be reduced by 60% at a current density of $8 \times 10^5$ A/cm$^2$. Furthermore, we show that the damping reduction has a strong dependence on spin-wave frequency and we demonstrate that this dependence arises from nonlinear magnon scattering.

DOI: 10.1103/PhysRevApplied.11.034046

## I. INTRODUCTION

Spin waves are coherent oscillations of spin in magnetic materials and have been used in tunable radio frequency (rf) filters that are based on Yttrium Iron Garnet (YIG) [1–4]. Spin waves have also been used for frequency selective limiters, signal-to-noise enhancers, and phase shifters, as well as logic operations [2,5–7]. However, damping remains a key factor in rf electronics that are based on thin YIG films. For practical rf applications where power handling is critical, thick YIG films ($> 1\ \mu$m) grown using liquid phase epitaxy (LPE) are preferred. A great deal of effort has been put into growing thick YIG films of ultralow damping [8,9], yet a finite amount of damping in these films still hinders practical spin-wave applications. One method to compensate the spin-wave damping is to transfer the angular momentum of spin-polarized electrons to spin waves [10–15]. In these spin-wave devices, a ferro- or ferrimagnetic (FM) layer that carries the spin wave is placed adjacent to a spin current source, typically generated through spin hall effect (SHE) in heavy metals such as Pt or W. In spin-wave devices based on YIG, spin orbit torque (SOT) takes place at the surface, where electrons scatter and experience magnetic exchange. Several groups have achieved a reduction of spin-wave damping rate in pulsed laser deposition (PLD)- [12,13] and LPE-grown [10,11,16] YIG using spin currents from Pt.

Here, we utilize a TI layer on a 2.3 $\mu$m thick LPE-grown YIG to reduce the damping rate of magnetostatic surface spin waves (MSSW) with the device shown in Fig. 1(a). TI is a special class of material where, in accord with the time-reversal symmetry (TRS), the spins of the Dirac-like surface states are locked to their momentum [17–24]. This results in spin polarized currents at the surfaces whereas the bulk remains semiconducting and, arguably, less spin polarized. Since SOT is a surface phenomenon, TI can potentially be more efficient in providing the antidamping torque, and thus be more efficient in reducing spin-wave damping compared with conventional heavy metals. In our experiments, we choose $Bi_2Se_3$ as the TI material with a thickness of 15 nm to avoid electronic hybridization between the two surfaces. Although there have been several studies on SOT in TI and FM metal layers [25–28], there have been fewer studies that have demonstrated

*aryan.n@ieee.org

 

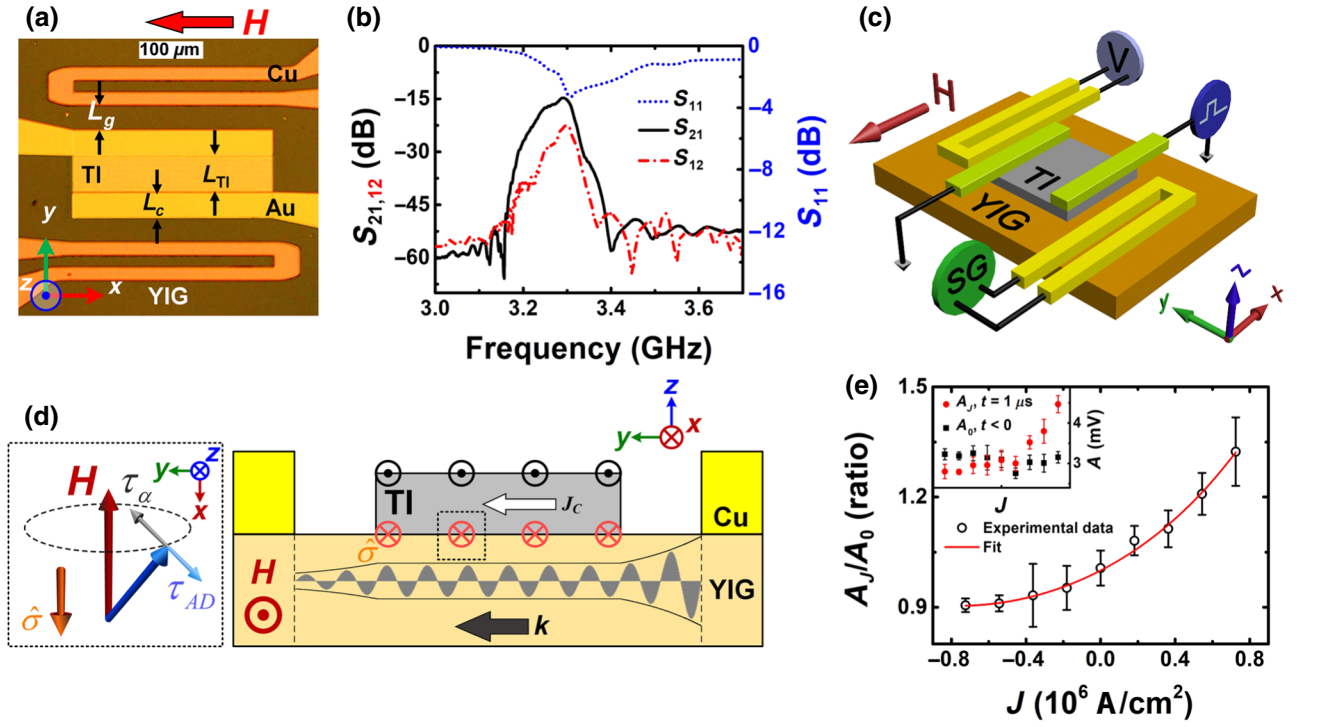


FIG. 1. Amplification of spin waves. (a) Optical image of the spin-wave device. (b) $S$ parameters of the spin-wave device measured using a VNA. (c) A SG launches a spin wave while a current pulse drives a spin-polarized current in the TI that enhances the spin-wave signal. (d) The spin currents from TI (with spin polarization $\hat{\sigma}$) transfer angular momentum to the spin wave with wavenumber $k$. Damping is compensated at a critical current density, $J_C$. (e) Spin-wave amplitude is controlled by spin currents from TI measured at 500 Oe and 3.39 GHz. The data is fitted (red solid line) using Eq. (2) (Inset: amplitude of the spin wave before and after the current pulse is applied).

interface effects in a YIG/TI system [29,30]. This could be mostly due to the challenges of growing a high-quality TI layer on a YIG substrate.

## II. EXPERIMENTAL DETAILS

An optical image of the device showing the dimensions is shown in Fig. 1(a) (for material growths and device fabrication see Secs. 1–3 in the Supplemental Material [31–35]). The transducers are shaped in a ground-signal-type coplanar waveguide (CPW) where both ground ($G$) and signal ($S$) lines, as well as the gap between them, have a width of 20 $\mu$m. The gaps between the transducers and the gold metal contacts ($L_g$) and the width of the gold contacts ($L_c$) are both 40 $\mu$m. The length of the TI layer ($L_{TI}$) is 60 $\mu$m and its width is 320 $\mu$m.

Figure 1(b) shows the Scattering- ($S$) parameters of the device obtained using a Vector Network Analyzer (VNA) with the magnetic field oriented along the $-x$ direction and set to 500 Oe. The $S_{11}$ parameter, which is observed to be the same as the $S_{22}$ parameter, is shown with the dotted blue line and it is indicative of the power absorbed by the YIG. The $S_{21}$ is shown with the solid black line and indicates the transmitted power. In our measurements, due to the geometry of our device, we observe both volume spin waves and surface spin waves, also known as Damon-Eshbach (DE) modes [36]. The $S_{12}$ (red dot-dashed line) shows a higher insertion loss because of nonreciprocity of surface spin waves [37–39].

Next, we drive a current through the TI layer as spin waves with a frequency of 3.39 GHz at $H = 500$ Oe are being continuously excited using a Signal Generator (SG) with an output power of 4 dBm. Figure 1(c) shows the schematic of the measurement set up. The amplitude of the propagating spin wave is measured using an oscilloscope, which we also use as a spectrum analyzer [40]. We use a 1-$\mu$s current pulse with a repetition period of 50 ms to reduce the Joule heating. The Oersted field generated by the conductive TI layer is calculated to be between 1 to 2 Oe at the highest current densities, which causes an insignificant change in the resonant frequency. Figure 1(d) illustrates the concept of using TI for transferring angular momentum from spin currents to spin waves in YIG. As spin waves propagate and decay due to the damping torque ($\tau_\alpha$), for a given direction of current, the antidamping torque ($\tau_{ad}$) caused by the spin currents (with spin polarization $\hat{\sigma}$) acts on the magnetization, preventing the spin-wave amplitude from further decay until it reaches

the other end of the TI layer. When a current of opposite direction is driven in TI, the spin polarization of the generated spin currents is reversed and thus SOT from TI further attenuates the spin-wave amplitude. The results are shown in Fig. 1(e). The gain is defined as the ratio of the spin-wave amplitude when a 1-$\mu$s current pulse is applied, $A_J$, over the amplitude before the current pulse is applied, $A_0$. Figure 1(e) shows gain for positive currents of up to 32% for a current density of $8 \times 10^5$ A/cm$^2$ and an attenuation of nearly 90% for negative currents of the same magnitude. The measured amplitudes of the spin wave before and after the current pulse are shown in the inset in Fig 1(e) using the black square and red circle markers, respectively. To analyze the gain of the spin-wave amplitude, we adopt the method used by E. Padrón-Hernández *et al.* [11,16] where the amplitude is expressed as

$$A(J) = A_J e^{-i\omega t} = c_k(0) e^{-i\omega t} e^{-(\eta_k - \alpha_k J - \beta_k \nabla T)t}, \quad (1)$$

where $c_k(0)$ is the initial spin-wave amplitude with wavenumber $k$, $\omega$ is the spin-wave angular frequency, $\eta_k$ is the spin-wave damping rate, $\alpha_k$ is the parameter related to SOT, and $J$ is the current density that is driven through the TI layer. $\beta_k$ is the parameter proportional to the Spin Seebeck Effect (SSE) and $\nabla T$ is the longitudinal temperature gradient across the film [16], which is proportional to $J^2$, which is considered to be small in our experiment since the pulse duration and duty cycle are very low (see Sec. 4 of the Supplemental Material [31]). The gain $G$ can be determined by

$$G(J) = \frac{A(J)}{A(0)} = e^{a(J/J_C + \nabla T/\nabla T_C)}, \quad (2)$$

where the prefactor $a$ is equal to $\eta_k L_{\mathrm{TI}}/v_g$ with $v_g$ being the group velocity. $J_C$ is the critical current density and is equal to $\eta_k/\alpha_k$. Based on this formulation, $J_C$ is essentially an extrapolated parameter and it is the current density at which the damping of the spin waves is entirely compensated [11,12,16,27,41–45]. Similarly, $\nabla T_C$ is also an extrapolated parameter, equal to $\eta_k/\beta_k$, and is defined as the temperature gradient at which the damping is compensated [16]. It should be noted that since there are gaps between the two transducers and the TI contacts that are equal to $2 \times (L_g + L_c)$, the spin current from the TI does not exert any torque on the spin waves within these gaps [see Figs. 1(a) and 1(d)]. Even if we use current densities equal to $J_C$, there will still be losses in this gap that we could not compensate for due to our device geometry. The losses under the gold contacts regions are even more significant because of the changes in the surface conductance and boundary conditions [39,46]. To be able to estimate $J_C$, the group velocity needs to be determined, which requires an accurate estimation of the wavenumber $k$ at the operating frequency. We will return to evaluating $J_C$ later in this paper.

We repeat the measurements done in Fig. 1(e) for frequencies ranging from 3.15 GHz to around 3.4 GHz. Figure 2(a) shows the spin-wave spectrum when no current is applied to the TI layer, that is, $J = 0$ A/cm$^2$. In Fig. 2(b), we show examples of the gain obtained at different frequencies. The figure clearly shows that the gain at the highest current density changes with frequency. To further illustrate this frequency dependence, we plot the maximum gain in dB obtained at the extreme current density values, $\pm 8 \times 10^5$ A/cm$^2$, vs frequency in Fig. 2(c). The red curve with the upward triangle data points shows the gain for $+8 \times 10^5$ A/cm$^2$ and the blue curve with the downward triangle data points shows the gain for $-8 \times 10^5$ A/cm$^2$. At frequencies close to 3.38 GHz, we observe a peak in the gain. The total gain is comprised of two components, one is due to SOT, the other due to SSE, which is an even function with respect to the current. To separate the SOT and the SSE contributions in the gain, we fit the data points in Fig. 2(b) for all frequencies to the exponential term in the gain equation [Eq. (2)]. We remove the $a\nabla T/\nabla T_C$ term in the exponent that is proportional to $J^2$, which corresponds to Joule heating that results in SSE, and only plot the gain in dB that is linearly dependent on $J$ in Fig. 2(d); we call this component of the gain $G_{\mathrm{odd}}$. $G_{\mathrm{odd}}$ is maximized at 3.38 GHz, roughly 100 MHz above the frequency of maximum spin-wave transmission, and the gain is almost zero elsewhere within the pass band.

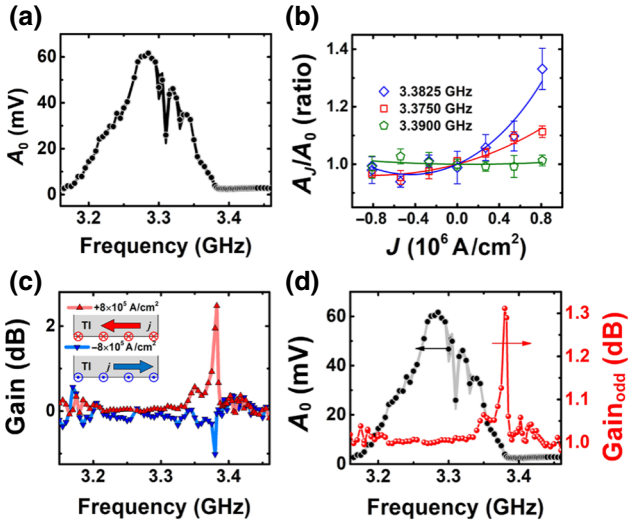


FIG. 2. Dependence of the gain on spin-wave frequency. (a) Spin-wave amplitude measured using an oscilloscope/spectrum analyzer with the external magnetic field set to 500 Oe. (b) Different spin-wave frequencies show different amounts of gain. The markers show experimental data and the solid lines are the fits to Eq. (2). (c) The dependence of total gain on spin-wave frequency is illustrated by plotting the maximum total gain in dB. The figure shows that the gain is more significant for a narrow range of frequencies above the maximum transmission frequency. (d) The gain due to SOT vs the spin-wave pass band.

## III. RESULTS AND DISCUSSION

In Fig. 3, we plot the total gain that is measured for $H = 450$, 500, 550, and 900 Oe. We see that in the cases of 450, 500, and 550 Oe, the gain is maximized for a narrow frequency range above the center of the pass band, while in the case of 900 Oe, no significant gain is observed even at frequencies 400 MHz above the maximum transmission frequency. We note that the frequency differences between the peak of maximum transmission and maximum gains we observe are different for the three magnetic fields, which shows that neither an Oersted field nor a field-like torque is the reason behind the shift in frequency. To understand the dependence of gain on spin-wave frequency and the external magnetic field, we use the VNA to measure the $S_{21}$ parameter for magnetic fields ranging from 400 to 600 Oe with steps of 2 Oe [see Fig. 4(a)]. The color scale represents the magnitude of the $S_{21}$ parameter in dB. Therefore, a vertical cut of this color plot, such as the one along the solid black line at 500 Oe, is a single measurement by the VNA shown in Fig. 1(b). One main feature in this figure is the red triangle that starts at 450 Oe and around 3 GHz. This region of the plot is indicative of high spin-wave transmission. Another set of features are the streaks that are parallel to the white dashed lines. These streaks are spin waves with unique wavenumbers that couple most efficiently to the transducers [47]. Therefore, by fitting the dispersion relation to these lines and using the thickness of YIG and an estimate value of $M_S$ from superconducting quantum interference device (SQUID) magnetometry, we can find the wavenumber for each individual frequency at a given magnetic field. Using the wavenumber, we can determine the group velocities and the critical current densities.

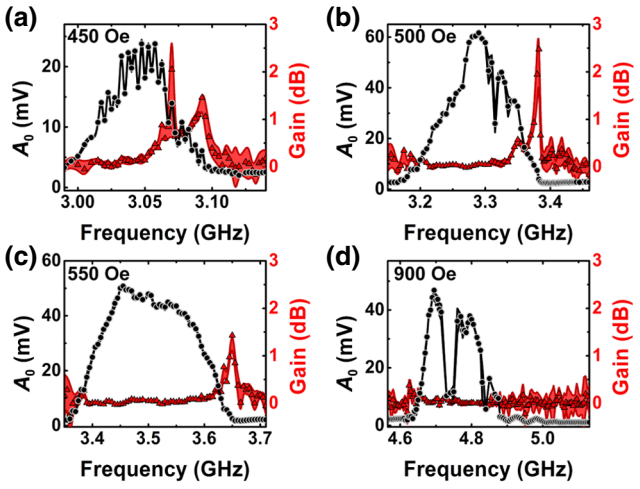


FIG. 3. Dependence of the gain enhancement on an external magnetic field. Spin-wave pass band spectrum (black circles) and total gain of spin-wave amplitude in dB (red triangles) with a current density of $8 \times 10^5$ A/cm$^2$ at 450 Oe (a), 500 Oe (b), 550 Oe (c), and 900 Oe (d). The data shown in (b) is the same as that in Figs. 2(a) and 2(c) (red upward triangles) for comparison. The total gain has a peak at some frequency above the maximum transmission frequency (a–c), whereas the total gain in (d) does not show any enhancement for frequencies 400 MHz above the maximum transmission frequency.

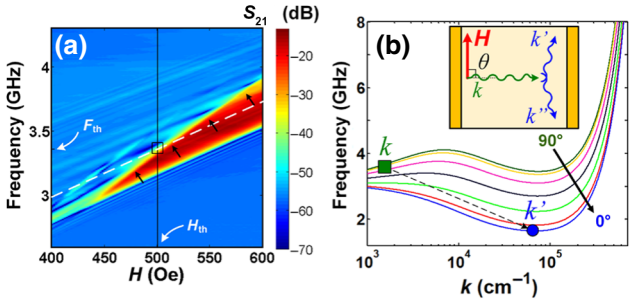


FIG. 4. Three-magnon scattering in YIG. (a) Experimental data showing the $S_{21}$ parameter for 500 Oe. The white dashed line is a spin wave with a wavenumber that crosses $F_{th} \approx 3.38$ GHz. The four black arrows highlight a line that separates the linear and nonlinear regions. For the spin wave with wavenumber corresponding to the white dashed line, beyond the magnetic field $H_{th}$ (solid black square), three-magnon scattering is suppressed and spin-wave transmission increases. (b) The dispersion curves for spin waves propagating at angles ranging from 0° to 90° with respect to $H$. The inset shows the scenario when a spin wave propagating at 90° (green rectangle) scatters to two other spin waves (blue circle).

As mentioned above, the red triangular feature in Fig. 4(a) represents high-spin-wave transmission. For a spin wave of a unique wavenumber, such as the one represented with the white dashed line, the spin-wave transmission increases once a threshold magnetic field and frequency, $H_{th}$ and $F_{th}$, respectively, are reached, in this case 500 Oe and about 3.38 GHz. This threshold magnetic field increases for higher wavenumbers and it always lies along the line marked with the four black arrows. This behavior allows for the assumption that three-magnon scattering [48–52] is being suppressed above the threshold field, thus enhancing the spin-wave transmission. This can be understood using Fig. 4(b), which shows the dispersion curves for spin waves excited at 500 Oe and propagating at angles $\theta$ ranging from just above 0° to 90° with respect to the external magnetic field $H$. For spin waves that are excited at a frequency and a wavenumber represented with the green square, they propagate at 90° at low but finite $k$ values. For such spin waves with frequency $f$, there exist states at wavenumber $k'$ with a frequency of approximately $f/2$ (blue circle) to which they can scatter. For the energy and momentum to be conserved, the spin wave also scatters to another state with a frequency close to $f/2$ with a negative wavenumber $k''$, not shown in Fig. 4(b), where $\vec{k} = \vec{k'} + \vec{k''}$. In the scenario shown in Fig. 4(b), the only states the spin waves can scatter to are the ones at the very bottom of the dispersion curve of spin

waves propagating almost parallel to the magnetic field. For magnetic fields higher than $H_{th}$, this scattering process is suppressed since there will be a frequency offset in all the curves along the positive frequency direction and the condition for energy conservation can no longer be satisfied. Since three-magnon scattering is a nonlinear process, it can be identified by comparing the measured insertion losses at different input powers. The power dependence of the $S_{21}$ parameter is measured and is shown in Sec. 5 of the Supplemental Material [31,53]. To further confirm that this feature stems from three-magnon scattering, we use the dispersion relation to estimate the frequencies and magnetic fields at which three-magnon scattering occurs (see Sec. 6 of the Supplemental Material [31]). Based on these results, we can conclude that the line marked by the four black arrows is the boundary between linear and nonlinear dynamics. It should be noted that the gain curves we observe in Figs. 2(d) and 3 are not artifacts caused by the Oersted field, which may shift the entire spin-wave spectrum. Near the three-magnon boundary, this effect may shift the spin waves from a low transmission nonlinear regime to a high transmission linear regime. If this is the case, one would observe a pair of gain peaks with opposite polarities on both sides of the maximum transmission frequency, which are not present in our experiments. Additionally, the Oersted field-induced spin-wave spectrum shift is estimated to be below 5 MHz, which is much narrower than the gain peak. This again rules out the Oersted field as the cause for our observed gain curve. The same results are also observed in devices with different geometries.

The important finding of this study is that the maximum gain measured at different magnetic fields occurs at their corresponding $F_{th}$ and on the boundary between linear and nonlinear dynamics. Thus, three-magnon scattering is the reason behind the frequency dependence of the gain. This hypothesis is supported by the input power-dependent gain measurements (see Sec. 7 of the Supplemental Material [31]), where the maximum gain occurring on the boundary between linear and nonlinear regimes reduces at decreasing input powers and becomes negligible at low input powers with suppressed three-magnon scattering. Spin waves at a frequency $F_{th}$ scatter to a very small phase space located at the bottom of the approximately 0° propagation angle dispersion curve in Fig. 4(b). A high population of low-energy magnons induced by the SOT can suppress and ultimately even reverse the three-magnon scattering process that drains the low $k$ modes. Such a reversal is expected at the onset of the SOT-induced condensation of magnons at the dispersion minima. The tendency of a pumped magnon gas to condense at the finite-momentum dispersion minima has been previously established in the case of parametric pumping [54–56].

Finally, we determine the critical current density, $J_C$, for the three magnetic fields where we measure maximum gain. As mentioned before, we use the parallel streaks in Fig. 4(a) and the dispersion relation to determine the wavenumber at the frequencies showing maximum gain as accurately as possible (see Sec. 8 of the Supplemental Material [31,39]). The results are shown in Fig. 5, where we also show a critical current density of $1.19 \times 10^6$ A/cm$^2$ at 450 Oe with a 60% reduction in the damping rate, $\Delta\eta$, at a current density of $8 \times 10^5$ A/cm$^2$. By taking the effect of the TI metal contacts on the dispersion relationship into account [34] we calculate $J_C$ to be $1.5 \times 10^6$ A/cm$^2$. This is smaller than that observed in the YIG/Pt bilayer [11], which is just above $2.16 \times 10^6$ A/cm$^2$ at 89 Oe, and is much smaller than values measured in micrometer-wide YIG films deposited using pulsed laser deposition (PLD) [13]. The results also indicate that the SOT process becomes less efficient at higher fields and more current is required to overcome the damping.

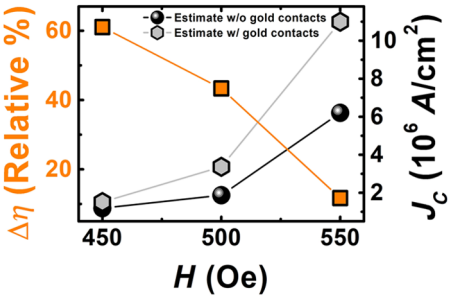


FIG. 5. The change in spin-wave damping rate, $\Delta\eta$ (orange squares) and critical current density, $J_C$ (black circles), for different external magnetic fields. At 450 Oe, the control of spin-wave damping rate is the most efficient where at $8 \times 10^5$ A/cm$^2$ 60% of the damping rate is reduced. This is also shown in the critical current density data where the value of $J_C$ is lowest at 450 Oe. The gray hexagonal markers are the critical current densities when group velocities are recalculated by taking the effect of the metal lines on the dispersion relationship into account. This increases $J_C$ at 450 Oe to $1.5 \times 10^6$ A/cm$^2$.

## IV. CONCLUSIONS

We demonstrate the reduction of spin-wave damping in YIG using spin currents from an adjacent TI layer. The spin-wave amplitude is amplified by 32% and by isolating the contribution of SSE, a gain due to SOT of 1.3 dB equivalent to a 16% gain in amplitude is achieved. Even if $Bi_2Se_3$ has a semiconducting bulk and thus the spin currents may have bulk contributions, the overall gain from both surface and bulk states is still higher than the 5% achieved in PLD YIG at the same current densities [13]. Due to three-magnon scattering, the frequency at which this peak gain is observed is above the pass band. The results indicate that the torque combined with the three-magnon scattering process leads to an efficient mechanism, which reduces spin-wave damping. In order to achieve

gain at the center frequency with the least amount of insertion loss, physical considerations such as three-magnon scattering and device geometry need to be considered and optimized. By uncovering these physical contributions and demonstrating the first YIG/TI system for control of spin-wave damping, this work paves the way for the utility of TI-produced SOT on magnetic insulators.

## ACKNOWLEDGMENTS

A.N. and Y.L. contributed equally to this work. Funding for the project was supported by DARPA M3IC program under contract through The Northrop Grumman Corporation. We would also like to thank Dr. Alexander A. Serga, Timo Noack from University of Kaiserlautern, and Dr. Vasil S. Tiberkevich from Oakland University for their discussion on the three-magnon scattering process and its role in the frequency dependence of the gain.

[1] F. R. Aramst, M. Grace, and S. Okwit, Low-level garnet limiters, Proc. IRE **49**, 1308 (1961).
[2] K. L. Kotzebue, Frequency-selective limiting, IRE Trans. Microw. Theory Tech. **10**, 516 (1962).
[3] S. Carter, Magnetically. Tunable single-crystal microwave filters using yttrium-iron-garnet resonators, IRE Trans. Microw. Theory Tech. **30**, 252 (1961).
[4] R. W. Degrasse, Low-loss gyromagnetic coupling through single crystal garnets, J. Appl. Phys. **30**, 155S (1959).
[5] E. Bankowski, T. Meitzler, R. S. Khymyn, V. S. Tiberkevich, A. N. Slavin, and H. X. Tang, Magnonic crystal as a delay line for low-noise auto-oscillators, Appl. Phys. Lett. **107**, 122409 (2015).
[6] J. D. Adam and S. N. Stitzer, A magnetostatic wave signal-to-noise enhancer, Appl. Phys. Lett. **36**, 485 (1980).
[7] M. P. Kostylev, A. A. Serga, T. Schneider, B. Leven, and B. Hillebrands, Spin-wave logical gates, Appl. Phys. Lett. **87**, 153501 (2005).
[8] R. C. Linares and E. L. Sloan III, Epitaxial growth of narrow linewidth yttrium iron garnet films, J. Cryst. Growth **27**, 249 (1974).
[9] H. J. Levinstein, S. Licht, R. W. Landorf, and S. L. Blank, Growth of highquality garnet thin films from supercooled melts growth of high-quality garnet thin films from supercooled melts, Appl. Phys. Lett. **19**, 486 (1971).
[10] Z. Wang, Y. Sun, M. Wu, V. Tiberkevich, and A. Slavin, Control of Spin Waves in a Thin Film Ferromagnetic Insulator Through Interfacial Spin Scattering, Phys. Rev. Lett. **107**, 146602 (2011).
[11] E. Padrón-Hernández, A. Azevedo, and S. M. Rezende, Amplification of spin waves in yttrium iron garnet films through the spin Hall effect, Appl. Phys. Lett. **99**, 192511 (2011).
[12] A. Hamadeh, O. D'Allivy Kelly, C. Hahn, H. Meley, R. Bernard, A. H. Molpeceres, V. V. Naletov, M. Viret, A. Anane, V. Cros, S. O. Demokritov, J. L. Prieto, M. Muñoz, G. De Loubens, and O. Klein, Full Control of the Spin-Wave Damping in a Magnetic Insulator Using Spin-Orbit Torque, Phys. Rev. Lett. **113**, 197203 (2014).
[13] M. Evelt, V. E. Demidov, V. Bessonov, S. O. Demokritov, J. L. Prieto, and M. Muñoz, High-efficiency control of spin-wave propagation in ultra-thin yttrium iron garnet by the spin-orbit torque, Appl. Phys. Lett. **108**, 172406 (2016).
[14] V. E. Demidov, S. Urazhdin, A. B. Rinkevich, G. Reiss, and S. O. Demokritov, Spin Hall controlled magnonic microwaveguides, Appl. Phys. Lett. **104**, 152402 (2014).
[15] K. An, D. R. Birt, C. F. Pai, K. Olsson, D. C. Ralph, R. A. Buhrman, and X. Li, Control of propagating spin waves via spin transfer torque in a metallic bilayer waveguide, Phys. Rev. B **89**, 140405 (2014).
[16] E. Padrón-Hernández, A. Azevedo, and S. M. Rezende, Amplification of spin waves by the spin Seebeck effect, J. Appl. Phys. **111**, 07D504 (2012).
[17] M. Z. Hasan and C. L. Kane, Colloquium: Topological insulators, Rev. Mod. Phys. **82**, 3045 (2010).
[18] Y. Fan and K. L. Wang, Spintronics based on topological insulators, Spin **06**, 1640001 (2016).
[19] J. E. Moore, The birth of topological insulators, Nature **464**, 194 (2010).
[20] X. L. Qi, T. L. Hughes, and S. C. Zhang, Topological field theory of time-reversal invariant insulators, Phys. Rev. B **78**, 195424 (2008).
[21] X. L. Qi and S. C. Zhang, Topological insulators and superconductors, Rev. Mod. Phys. **83**, 1057 (2011).
[22] H. Zhang, C.-X. Liu, X.-L. Qi, X. Dai, Z. Fang, and S.-C. Zhang, Topological insulators in $Bi_2Se_3$, $Bi_2Te_3$ and $Sb_2Te_3$ with a single Dirac cone on the surface, Nat. Phys. **5**, 438 (2009).
[23] J. E. Moore and L. Balents, Topological invariants of time-reversal-invariant band structures, Phys. Rev. B **75**, 121306 (2007).
[24] C. L. Kane and E. J. Mele, Z2 Topological Order and the Quantum Spin Hall Effect, Phys. Rev. Lett. **95**, 146802 (2005).
[25] M. Jamali, J. S. Lee, J. S. Jeong, F. Mahfouzi, Y. Lv, Z. Zhao, B. K. Nikolić, K. A. Mkhoyan, N. Samarth, and J. P. Wang, Giant spin pumping and inverse spin Hall effect in the presence of surface and bulk spin-orbit coupling of topological insulator $Bi_2Se_3$, Nano Lett. **15**, 7126 (2015).
[26] J. Han, A. Richardella, S. A. Siddiqui, J. Finley, N. Samarth, and L. Liu, Roomerature Spin-Orbit Torque Switching Induced by a Topological Insulator, Phys. Rev. Lett. **119**, 077702 (2017).
[27] A. A. Baker, A. I. Figueroa, L. J. Collins-McIntyre, G. van der Laan, and T. Hesjedal, Spin pumping in ferromagnet-topological insulator-ferromagnet heterostructures, Sci. Rep. **5**, 7907 (2015).
[28] A. R. Mellnik, J. S. Lee, A. Richardella, J. L. Grab, P. J. Mintun, M. H. Fischer, A. Vaezi, A. Manchon, E. A. Kim, N. Samarth, and D. C. Ralph, Spin-transfer torque generated by a topological insulator, Nature **511**, 449 (2014).
[29] M. Lang, M. Montazeri, M. C. Onbasli, X. Kou, Y. Fan, P. Upadhyaya, K. Yao, F. Liu, Y. Jiang, W. Jiang, K. L. Wong, G. Yu, J. Tang, T. Nie, L. He, R. N. Schwartz, Y. Wang, C. A. Ross, and K. L. Wang, Proximity induced high-temperature magnetic order in topological insulator - Ferrimagnetic insulator heterostructure, Nano Lett. **14**, 3459 (2014).

[30] Z. Jiang, C. Z. Chang, C. Tang, P. Wei, J. S. Moodera, and J. Shi, Independent tuning of electronic properties and induced ferromagnetism in topological insulators with heterostructure approach, Nano Lett. **15**, 5835 (2015).

[31] See Supplemental Material at http://link.aps.org/supplemental/10.1103/PhysRevApplied.11.034046 for details on sample preparation, characterization, calculation and measurment details.

[32] X. Liang, Y. Zhu, B. Peng, L. Deng, J. Xie, H. Lu, M. Wu, and L. Bi, Influence of interface structure on magnetic proximity effect in $Pt/Y_3Fe_5O_{12}$ heterostructures, ACS Appl. Mater. Interfaces **8**, 8175 (2016).

[33] Y. Kubota, K. Murata, J. Miyawaki, K. Ozawa, M. C. Onbasli, T. Shirasawa, B. Feng, S. Yamamoto, R. Y. Liu, S. Yamamoto, S. K. Mahatha, P. Sheverdyaeva, P. Moras, C. A. Ross, S. Suga, Y. Harada, K. L. Wang, and I. Matsuda, Interface electronic structure at the topological insulator-ferrimagnetic insulator junction, J. Phys. Condens. Matter **29**, 055002 (2017).

[34] Z. Qiu, K. Ando, K. Uchida, Y. Kajiwara, R. Takahashi, H. Nakayama, and T. An, Spin mixing conductance at a well-controlled platinum/yttrium iron garnet interface, Appl. Phys. Lett. **103**, 092404 (2013).

[35] Z. Jiang, C. Z. Chang, C. Tang, J. G. Zheng, J. S. Moodera, and J. Shi, Structural and proximity-induced ferromagnetic properties of topological insulator-magnetic insulator heterostructures, AIP Adv. **6**, 055809 (2016).

[36] C. W. Sandweg, Y. Kajiwara, K. Ando, E. Saitoh, and B. Hillebrands, Enhancement of the spin pumping efficiency by spin wave mode selection, Appl. Phys. Lett. **97**, 252504 (2010).

[37] S. O. Demokritov, B. Hillebrands, and A. N. Slavin, Brillouin light scattering studies of confined spin waves: Linear and nonlinear confinement, Phys. Rep. **348**, 441 (2001).

[38] T. Schneider, A. A. Serga, B. Leven, B. Hillebrands, R. L. Stamps, and M. P. Kostylev, Realization of spin-wave logic gates, Appl. Phys. Lett. **92**, 022505 (2008).

[39] D. D. Stancil and A. Prabnakar, *Spin Waves* (Springer, New York, NY, 2009).

[40] A. A. Serga, A. B. Chumak, and B. Hillebrands, YIG magnonics, J. Phys. D: Appl. Phys. **43**, 264002 (2010).

[41] A. Slavin and V. Tiberkevich, Nonlinear auto-oscillator theory of microwave generation by spin-polarized current, Adv. Magn. **45**, 1875 (2009).

[42] V. E. Demidov, S. Urazhdin, E. R. J. Edwards, M. D. Stiles, R. D. McMichael, and S. O. Demokritov, Control of Magnetic Fluctuations by Spin Current, Phys. Rev. Lett. **107**, 107204 (2011).

[43] M. Collet, X. de Milly, O. d'Allivy Kelly, V. V. Naletov, R. Bernard, P. Bortolotti, J. Ben Youssef, V. E. Demidov, S. O. Demokritov, J. L. Prieto, M. Muñoz, V. Cros, A. Anane, G. de Loubens, and O. Klein, Generation of coherent spin-wave modes in yttrium iron garnet microdiscs by spin-orbit torque, Nat. Commun. **7**, 10377 (2016).

[44] Y. Tserkovnyak, A. Brataas, and G. E. W. Bauer, Theory of current-driven magnetization dynamics in inhomogeneous ferromagnets, J. Magn. Magn. Mater. **320**, 1282 (2008).

[45] I. N. Krivorotov, N. C. Emley, J. C. Sankey, S. I. Kiselev, D. C. Ralph, and R. a Buhrman, Time-domain measurements of nanomagnet dynamics driven by spin-transfer torques, Science **307**, 228 (2005).

[46] A. G. Gurevich and G. A. Melkov, *Magnetization Oscillations and Waves* (CRC Press, Boca Raton, FL, 1996).

[47] V. Vlaminck and M. Bailleul, Spin-wave transduction at the submicrometer scale: Experiment and modeling, Phys. Rev. B **81**, 014425 (2010).

[48] H. Kurebayashi, O. Dzyapko, V. E. Demidov, D. Fang, A. J. Ferguson, and S. O. Demokritov, Controlled enhancement of spin-current emission by three-magnon splitting, Nat. Mater. **10**, 660 (2011).

[49] M. Sparks, R. Loudon, and C. Kittel, Ferromagnetic relaxation. I. Theory of the relaxation of the uniform precession and the degenerate spectrum in insulators at low temperatures, Phys. Rev. **122**, 791 (1961).

[50] P. Pincus, M. Sparks, and R. C. Lecraw, Ferromagnetic relaxation. II. The role of four-magnon processes in relaxing the magnetization in ferromagnetic insulators, Phys. Rev. **124**, 1015 (1961).

[51] C. L. Ordóñez-Romero, B. A. Kalinikos, P. Krivosik, W. Tong, P. Kabos, and C. E. Patton, Three-magnon splitting and confluence processes for spin-wave excitations in yttrium iron garnet films: Wave vector selective Brillouin light scattering measurements and analysis, Phys. Rev. B **79**, 144428 (2009).

[52] J. A. C. Bland and B. Heinrich, *Ultrathin Magnetic Structures* (Springer, Berlin, 1994).

[53] B. A. Kalinikos, M. P. Kostylev, N. V. Kozhus, and A. N. Slavin, Theory of dipole-exchange spin wave spectrum for ferromagnetic films with mixed exchange boundary conditions, J. Phys. C Solid State Phys. **19**, 7013 (1986).

[54] S. O. Demokritov, V. E. Demidov, O. Dzyapko, G. A. Melkov, A. A. Serga, B. Hillebrands, and A. N. Slavin, Bose-Einstein condensation of quasi-equilibrium magnons at room temperature under pumping, Nature **443**, 430 (2006).

[55] E. R. J. Edwards, H. Ulrichs, V. E. Demidov, S. O. Demokritov, and S. Urazhdin, Parametric excitation of magnetization oscillations controlled by pure spin current, Phys. Rev. B - Condens. Matter Mater. Phys. **86**, 134420 (2012).

[56] V. Lauer, D. A. Bozhko, T. Brächer, P. Pirro, V. I. Vasyuchka, A. A. Serga, M. B. Jungfleisch, M. Agrawal, Y. V. Kobljanskyj, G. A. Melkov, C. Dubs, B. Hillebrands, and A. V. Chumak, Spin-transfer torque based damping control of parametrically excited spin waves in a magnetic insulator, Appl. Phys. Lett. **108**, 012402 (2016).